


First-order localization and quantum phase transition induced by quasicrystal imaginary domain

Xianqi Tong  and Su-Peng Kou ^{*}

Department of Physics, Beijing Normal University, Beijing 100000, People's Republic of China



(Received 9 October 2023; accepted 15 February 2024; published 22 March 2024)

The non-Hermitian extension of quasicrystals provides a highly tunable system for exploring novel material phases. While extended-localized phase transitions have been observed in one dimension, quantum phase transitions in higher dimensions and various system sizes remain unexplored. Here, we show the discovery of a new critical phase and first-order structural transition induced by imaginary zeros in the two-dimensional Haldane model with a quasicrystal potential on the upper boundary. Initially, we illustrate a phase diagram that evolves with the amplitude and phase of the quasicrystal potential, which is divided into three distinct phases by two critical boundaries: phase (I) with extended wave functions, parity-time-restore phase (II) with localized wave functions, and a critical phase (III) with multifunctional wave functions. To characterize the wave functions in these distinct phases, we introduce a low-energy approximation theory and an effective two-chain model. Additionally, we uncover a first-order quantum phase transition induced by quasicrystal domains. As we increase the size of the potential boundary, we observe the partitioning of the critical phase into regions in proportion to the growing number of quasicrystal domains. Importantly, these observations are consistent with ground state fidelity and energy gap calculations. Our research advances the understanding of phase diagrams associated with high-dimensional quasicrystal potentials and marks the first discovery of a first-order quantum phase transition induced by quasicrystal domains in non-Hermitian systems.

DOI: [10.1103/PhysRevResearch.6.013314](https://doi.org/10.1103/PhysRevResearch.6.013314)

I. INTRODUCTION

The exploration of open systems, characterized by non-Hermitian quantum systems, has unraveled intriguing phenomena absent in their Hermitian counterparts [1–13]. Notable examples include parity-time (PT) symmetry and exceptional points [4–10], non-Bloch bulk-boundary correspondence [7,11], and non-Hermitian skin effects [7,11,13–21]. Many of these phenomena are related to PT-symmetric Hamiltonians. These Hamiltonians typically exhibit two phases as parameters vary: the PT-symmetric phase with real eigenvalues and the PT-breaking phase with complex eigenvalues [2–5]. These phenomena have been experimentally observed in open systems [22–29], with promising applications in precision measurements, nonreciprocal quantum devices, and topological transport. The higher-order nontrivial interplay between the non-Hermitian skin effect and the topological effect has led to the concept of a hybrid skin-topological effect [30–35].

Quasicrystals (QCs) in closed quantum systems exhibit a plethora of fascinating properties [36–44]. For instance, in the one-dimensional (1D) Aubry-André-Harper (AAH) model,

the introduction of finite quasicrystal strength leads to a transition from a metallic (extended) state to an Anderson insulator (localized) [36,45–47]. Critical phases are vital for understanding the transitions from localized to extended states, showing a range of fascinating phenomena including dynamical evolutions [48–50], critical spectral behavior [51–54], and the multifractal nature of wave functions [55–58]. To date, critical phases are possible in a few theoretical models, typically characterized by the 1D extensions of the AAH model with incommensurate nondiagonal hopping, p -wave superconductivity, and on-site potential [58–61]. Expanding upon the AAH model, variations incorporating different forms of quasidisorder and interactions give rise to exotic phases, including critically localized states [62–66] and many-body localization [67–69]. Recent research on non-Hermitian extensions of the 1D AAH model has uncovered such a multicritical point marking the transition from localized to extended states, accompanied by PT symmetry breaking and topological phase transitions [66,70,71]. Additionally, there is a growing interest in studying the influence of quasicrystals on 2D topological insulators [72–74]. However, the investigation of the interplay between the 2D chiral topological insulators and the non-Hermitian quasicrystal dissipation boundary has not been previously explored.

In this letter, our study not only reveals a complex phase diagram, but also establishes a profound relationship between the size of the non-Hermitian quasicrystal, the presence of imaginary zeros, and the occurrence of first-order quantum phase transitions (FOQPT). In the phase diagram, there are three distinct phases separated by two-phase boundaries: the

^{*}spkou@bnu.edu.cn

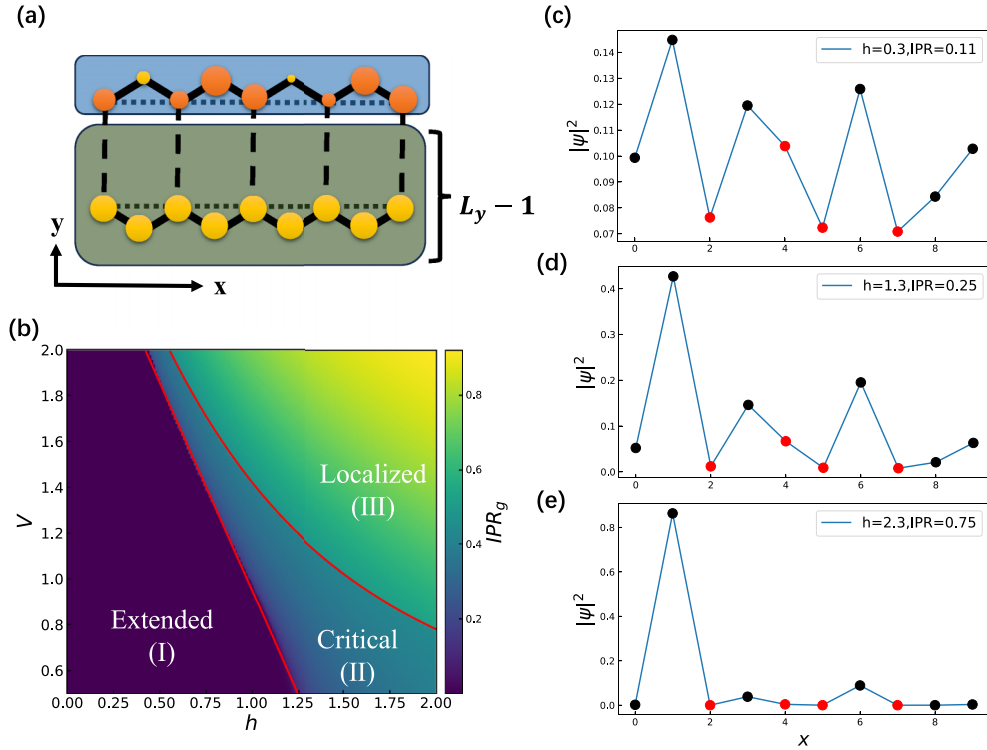


FIG. 1. [(a)–(e)] xPBC/yOBC. (a) Schematic of the 2D Haldane model with quasicrystal imaginary potential on the upper boundary. Quasicrystal and zero potentials are denoted by orange/yellow spheres against blue/green backgrounds, respectively. Black solid lines represent NN hopping, black dotted lines represent NNN hopping, and black dashed lines indicate intermediate hidden layers ($L_y - 1$). (b) The IPR as a function of V and h , reveals three phases separated by two critical lines: phase (I) with extended wave functions, PT-restored phase (III) featuring spatially localized wave functions, and critical phase (II) with fractional wave functions. Parameters: $L_x = 20$, $L_y = 20$. Two red phase transition lines represent our fitted results for $h_1 = -0.55 V + 1.52$, $h_2 = \log(3/V) + 0.44/(V^{1.6})$. [(c)–(e)] The density $|\psi|^2$ as functions of x at three distinct points, $h = 0.3, 1.3, 2.3$, with $V = 1$, following Eq. (8). (c) IPR=0.11, (d) IPR=0.25, (e) IPR=0.75.

extended phase (I), the localized phase (III), and the critical phase (II), see Fig. 1(b). Furthermore, our study uncovers, for the first time, the emergence of a FOQPT induced by quasicrystal imaginary domains in non-Hermitian systems. As the size of non-Hermitian quasicrystals increases, we observe a linear growth in the number of phase transitions (N_{QPT}). Firstly, within the quasicrystal potential, there are sites where the imaginary potential drops to zero. As the system’s parameters increase, such as amplitude and phase, this leads to the occurrence of a FOQPT [75,76]. Secondly, as the size of the system grows, the number of points with zero potential increases. These zero points divide the imaginary potential into distinct domains, and with varying parameters, each domain exhibits different phase transition points. Consequently, the N_{QPT} increases with the size of the system. We find that the N_{QPT} is equivalent to the number of zero points, which also matches the count of non-Hermitian domains.

The paper is organized as follows. In Sec. II, we construct the phase diagram using the inverse participation ratio and offer an interpretation based on the low-energy approximation. In Sec. III, we discuss the relationship between general imaginary domains and quasicrystal domain. In Sec. IV, we explore the impact of system size on the first-order quantum phase transition. Section V is devoted to our conclusion.

II. MODEL AND PHASE DIAGRAM

The foundation of our study lies in the Hamiltonian, which exhibits different forms under varying conditions:

$$H = \begin{cases} H_{AAH}, & L_y = 1 \\ \text{two-chains}, & L_y = 2, \\ H_{\text{Haldane}} + H_{AAH}^{\text{edge}}, & L_y \rightarrow \infty, \end{cases} \quad (1)$$

with two critical points of y direction dimensions $L_y = 1, 2$. When $L_y = 1$, the system returns back to the 1D non-Hermitian AAH model which plays a key role in this paper [66,71],

$$H_{AAH}^{\text{edge}} = \sum_n V \cos(2\pi\alpha n + ih) c_n^\dagger c_n, \quad (2)$$

where c_n^\dagger and c_n are the creation and annihilation operators for a particle at the n -th site. V and h are the amplitude and imaginary phase of the potential, respectively, and α is an irrational number for a QC. We set $V = 1$ as the energy unit without changing the results.

Since α is an irrational number, it can be approximated by a sequence of rational numbers p_n/q_n , where p_n, q_n are prime numbers and $p_n, q_n \rightarrow \infty$ as $n \rightarrow \infty$. In numerical simulations, it is common practice to consider a finite (yet arbitrarily large) number of sites $L = q_n$ on a ring with periodic boundary conditions.

Here we focus on the non-Hermitian Haldane model with quasicrystal imaginary potential $H_{\text{edge}}^{\text{AAH}}$ along the upper boundary [Fig. 1(a)], where height and circumference are L_y and L_x . In the limits $L_y \rightarrow \infty$, the Hamiltonian $H = H_{\text{Haldane}} + H_{\text{edge}}^{\text{AAH}}$ and the Haldane model is an important model for describing the topological insulator [45,77],

$$H_{\text{Haldane}} = t_1 \sum_{\langle nm \rangle} c_n^\dagger c_m + t_2 \sum_{\langle\langle nm \rangle\rangle} e^{i\phi_{nm}} c_n^\dagger c_m, \quad (3)$$

where the nearest-neighbor (NN) couplings are denoted by $t_1 = 1$, and the next-nearest-neighbor (NNN) coupling coefficients are $t_2 e^{i\phi_{nm}}$ with amplitude $t_2 = 0.2$ and phase ϕ_{nm} . The symbols $\langle n, m \rangle$ and $\langle\langle n, m \rangle\rangle$ denote the NN and NNN hopping, shown in Fig. 1(a) as black solid and black dotted lines, respectively. The complex phase $e^{i\phi_{nm}}$ accounts for the NNN hopping, and we set the positive phase direction to be clockwise ($|\phi_{nm}| = \frac{\pi}{2}$). Below, we consider periodic boundary condition (PBC) along the x direction and open boundary condition (OBC) along the y direction, i.e., a cylindrical geometry.

So far, the critical phases have only been found in the 1D AAH model with on-site potential, p -wave superconductivity, and incommensurate nondiagonal hopping [58–61]. However, we are the first to explore the impact of 2D non-Hermitian quasicrystal boundaries and to uncover the emergence of a critical phase. To determine the phase diagram of the Hamiltonian (1) under $L_y \rightarrow \infty$ condition, we compute the inverse of the participation ratio (IPR)

$$\text{IPR}_n = \frac{\sum_m |\psi_{n,m}|^4}{(\sum_m |\psi_{n,m}|^2)^2} \quad (4)$$

as a function of V and h , shown in Fig. 1(b). Here, $|\psi_{n,m}\rangle$ represents the eigenstate of the H corresponding to the energy eigenvalue E_n , and $m = 1, \dots, 2L_x$. Specifically, when n corresponds to the ground state (denoted as g), $|\psi_g\rangle$ represents the ground state, and IPR_g quantifies the localization of the ground state. Phase (I) with delocalized states has an $\text{IPR}_g \simeq 1/L \simeq 0$, the PT-restore phase (III) with fully localized states, on the other hand, has an $\text{IPR}_g \simeq 1$, and the critical phase (II) with fractional states fall in between, with IPR_g values ranging from 0 to 1, as shown in Fig. 1(b). Furthermore, the two red phase transition lines represent our fitted results for

$$h_1 = -0.55 V + 1.52, \quad h_2 = \log(3/V) + 0.44/(V^{1.6}). \quad (5)$$

Two critical lines are evident: the extended-critical transition line h_1 and the critical-localized phase transition line h_2 . In contrast to the 1D case, where only a transition from the extended phase to the localized phase is observed [66,70,71], and distinct from the mobility edge resulting from the coupling of two chains [58], our scenario gives rise to a novel critical phase.

Besides, we observe FOQPTs accompanied by the extended-critical and critical-localized transitions in a 2D Haldane model with an imaginary potential boundary, as in Appendix A.

Before proceeding with the discussion, we first clarify the wave functions of topological materials with imaginary potential boundaries. For a 2D chiral topological insulator, chiral modes can only exist on the boundary of topological

materials. In the continuous limit, the effective Hamiltonian in the low-energy approximation is described as $H_{\text{chiral}} = v_f k$, where $v_f = \frac{\partial H_{\text{chiral}}}{\partial k} \Big|_{k=k_f}$ is the Fermi velocity, and k is the vector of the chiral modes. In the long-wavelength and low-frequency regimes, excitations are restricted to one-direction propagation and protected by nontrivial bulk topology. The utilization of the low-energy approximation in describing the localization properties of wave functions at the boundary stems from the fact that, apart from variations in localized phases, the extended and critical phases closely resemble the ground state phase diagram. Should we consider the system to be in a topologically trivial phase, it has minimal impact on the phase diagram, as topological edge states exert negligible influence on the overall phase diagram.

Then, we consider the effects of dissipation which the boundary potential has a nonzero imaginary part, and the effective low-energy Hamiltonian [33–35] becomes

$$H_{\text{chiral}} = v_f k + iV, \quad (6)$$

where the imaginary part of eigenvalues is dependent on the on-site dissipation potential V . The Schrödinger equation of the dissipation chiral modes is

$$\left[-iv_f \frac{d}{dx} + iV(x) \right] \psi(x) = (\epsilon_r + i\epsilon_i) \psi(x), \quad (7)$$

where ϵ_i and ϵ_r represent the imaginary and real part of the eigenenergy, respectively.

Then, we get the solution of Eq. (7)

$$\psi(x) = \frac{1}{\sqrt{C}} \exp\left(i \frac{\epsilon_r}{v_f} x\right) \exp\left(\int_0^{L_x} dx' \frac{V(x') - \epsilon_i}{v_f}\right), \quad (8)$$

where $1/\sqrt{C}$ is the normalization factor and the integration region $(0, L_x)$ is on the dissipation boundary.

Since the 2D Haldane model is periodic in the x direction, the periodic boundary condition gives $\psi(L_x) = \psi(0)$. Then, we have

$$i \frac{\epsilon_r}{v_f} L_x - \frac{\epsilon_i}{v_f} L_x + \frac{1}{v_f} \int_0^{L_x} dx' V(x') = 2i\pi n, \quad (9)$$

where $n \in \mathbb{Z}$. Then, the Eq. (9) can be reduced to

$$\epsilon_r = \frac{1}{v_f} \frac{2\pi n}{L_x}, \quad (10)$$

$$\epsilon_i = \frac{1}{L_x} \int_0^{L_x} dx' V(x') = \tilde{V}, \quad (11)$$

where the imaginary part of eigenenergy ϵ_i is the average value of imaginary potential \tilde{V} .

The first two components in Eq. (8), similar to plane waves $\exp(ikx)$, are uniformly distributed throughout the entire space. However, if the sign of v_f is fixed, exponential growth or decay is possible for the third component (8), depending on the sign of $\text{sgn}(V(x) - \epsilon_i)$ (either 1 or -1). For example, at position x_c , a steplike change in the sign of the imaginary potential occurs, specifically when $V(x < x_c) < 0$ to $V(x > x_c) > 0$. If combined with $v_f < 0$, the edge state will exhibit a peak at x_c . Similarly, if $V(x < x_c) > 0$ and $V(x > x_c) < 0$, and $v_f > 0$, the edge wave function will also display a peak at x_c . This behavior is depicted by the black (for positive imaginary potentials) and red (for negative imaginary

potentials) circles in Figs. 1(c)–1(e). These circles visually represent the locations where the edge state wave functions peak, corresponding to changes in the sign of the imaginary potential.

In the specific case of our study, the dissipative potential takes the form of a quasicrystal pattern [Eq. (2)]. Substituting Eq. (2) into Eq. (11), it can be reduced to

$$\epsilon_i = -\frac{V \sin^2(\pi \alpha L_x)}{\pi \alpha L_x} \sinh(h). \quad (12)$$

This leads to a periodic peak in the imaginary potential, as depicted in Figs. 1(c)–1(e). For a detailed view of the phase diagram in various phases [Fig. 1(b)] in different phases, we examine three points along the $V = 1$ line in Fig. 1(b): $h = 0.3, 1.3, 2.3$. As shown in Fig. 1(c), when the imaginary phase $h = 0.3$, the overall density of the wave function exhibits minor fluctuations along the x direction, corresponding to $\text{IPR} = 0.11 \approx 1/L_x$. As h increases to 1.3, the wave function's density varies more significantly, resulting in $\text{IPR} = 0.25$, indicating a wave function reminiscent of a fractal-like state, as shown in Fig. 1(d). Finally, for a larger imaginary phase $h = 2.3$, the low-energy approximation becomes less effective, yet it remains useful for describing eigenstates at the boundaries. The wave function shows random localization, with the maximum density $|\psi|_{\max}^2 \approx 0.9$ is observed at $L_x = 1$ ($\text{IPR} = 0.75$). Sharp peaks in the wave function are observed at black (positive) circles, see Fig. 1(e).

At $V = 1$, the extended-critical transition point at $h_1 = 0.97$ and the critical-localized phase transition at $h_2 = 1.41$. In Appendix B, for a more comprehensive analysis of the phase diagram, we calculate various physical quantities, including the fractional dimension, the maximum imaginary part of the topological edge states, the scaling exponent, and the ground state fidelity. These calculations served to elucidate the phase transitions at h_1 and h_2 . Besides, when $L_y = 2$, we construct an effective Hamiltonian, transforming the system from a 2D to a two-chain system composed of 1D AAH chain and free chain [54,78]. This allowed us to capture the main physical properties of the system. Moreover, we have also introduced modifications to the phase, hopping, and mass term, both of which do not affect the critical phase. Our findings suggest that the emergence of critical phases is unrelated to these parameters but is primarily a consequence of the coupling between localized states and extended states [54]. This allowed us to investigate the impact of the system's size along the y direction, leading to a deeper insight into the critical phase.

III. IMAGINARY AND QUASICRYSTAL DOMAIN

Imaginary domains provide a general approach to understanding the wave function and FOQPT in the system. Imaginary domain walls act similarly to finite potential wells, imposing constraints on the wave function akin to forming distinct spatial boundaries. As parameters change, the ground state tends to localize in the potential well with the lowest energy, while excited states localize in higher energy wells. At the critical point, the system undergoes a PT phase transition. After the PT phase transition, the wave functions are distributed only within the corresponding domain walls, and

the energy band shows an imaginary line gap, as shown in Fig. 2(a).

Furthermore, we observe that when multiple domain walls are present, the wave function is correspondingly restricted within these separate domains. Subsequently, we consider

$$H_{NNN} = H_{\text{Hermitian}} + iV_1 + iV_2/4, \quad V_1 = V_2, \quad (13)$$

where $H_{\text{Hermitian}} = \sum_n c_n^\dagger c_n + \text{H.c.}$ is a free chain. $V_1 = V \sum_{n=1}^{\frac{L}{4}} x_n$, $V_2 = V \sum_{n=\frac{3L}{4}}^L x_n$ are the first and second domains respectively, and V is the strength of imaginary domain.

In Fig. 2(a), the ground state wave function is depicted, with the positions of the first V_1 and second V_2 domains marked by yellow and green lines, respectively. In the left image, the ground state wave function is an extended state. However, as the imaginary potential strength V increases, the ground state wave function becomes progressively confined to the central region. Due to the presence of imaginary potentials at both ends, the potential energy is lowest in the middle, so the ground state wave function is mainly distributed in the middle. This effect becomes more pronounced with stronger imaginary potentials.

It is noteworthy that the domain walls here are two non-adjacent imaginary domain walls. With the variation in the strength V of the imaginary domains, two PT phase transitions occur, ultimately presenting two imaginary line gaps, as seen in Appendix C. We also discuss the scenario with adjacent domains, which results in only one PT phase transition, as shown in Fig. 9 from Appendix C.

We find that the quasicrystal imaginary potential in Eq. (2) represents a special type of imaginary domain. Due to the quasicrystal varying strength of the imaginary potential, points where the potential is approximately zero emerge, effectively demarcating different imaginary domains. As depicted below Fig. 2(a), for $L_x = 20$, two imaginary domains are present with boundaries at $x = 18$ and $x = 42$, marked by yellow and blue dashed lines, respectively. At $h=0.6$, the ground state remains an extended state. Upon reaching $h = 1.2$, the system undergoes its first PT phase transition. In the middle panel, where $h_1 < h < h_2$, the second domain has a lower average potential, causing the ground state to predominantly occupy the second domain area (18, 42), making it a critical wave function. $h = 1.7 > h_2$ corresponding to the right panel, the system has passed through the second PT phase transition into a localized phase. However, the ground state does not remain in the same domain but shifts to the first domain (0, 18). This is attributed to a level crossing in the Haldane model with quasicrystal domains on the boundary, a scenario distinct from 1D AAH models, where coupling between extended and localized states is absent [54]. The first domain, which has lower potential energy before the first PT transition, becomes higher in potential energy than the second domain. Consequently, what was an excited state in the first domain becomes the ground state, indicating a FOQPT. This is a situation distinct from the typical cases where imaginary potentials induce PT phase transitions. It is noteworthy that the presence of two quasicrystal domains (imaginary domains) leads to two FOQPTs (PT transitions). This phenomenon can be extended to

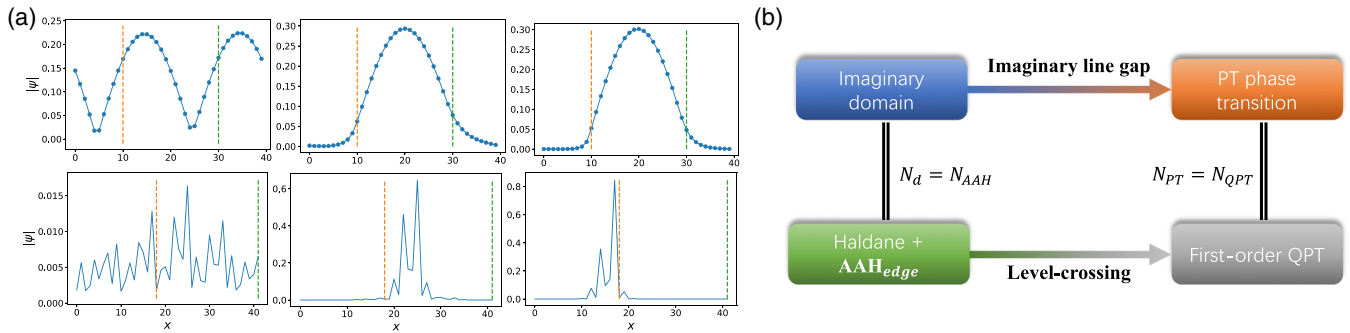


FIG. 2. (a) The top row presents the ground state of a one-dimensional free chain with nonadjacent quasicrystal domains. The three plots correspond to $V = 0.01, 0.80, 2.00$, respectively. The bottom row showcases the ground state of the Hamiltonian in Eq. 2, with the three plots corresponding to $h = 0.60, 1.20, 1.70$. In these plots, the yellow and green dashed lines indicate the positions of the first and second domains, respectively. (b) The relationship between quasicrystal domains, phase transitions, and quasiperiodic domain-induced first-order quantum phase transitions (QPTs): The quantities of imaginary domains (N_d), PT phase transitions (N_{PT}), quasicrystal domains (N_{AAH}) and quasicrystal domains inducing first-order quantum phase transitions (N_{QPT}) are all mutually equal, i.e., $N_{AAH} = N_d = N_{PT} = N_{QPT}$.

systems with more domains, as illustrated in Fig. 2(b):

$$N_{AAH} = N_d = N_{PT} = N_{QPT}, \quad (14)$$

where N_{AAH} , N_d , N_{PT} , N_{QPT} represent the number of quasicrystal domains, domains, PT phase transitions, and FOQPTs, respectively. In other word, $N_{AAH} = N_{QPT}$. In the following text, we will discuss the relationship between multiple quasicrystal domains and FOQPTs.

IV. FIRST-ORDER QUANTUM PHASE TRANSITION

In our study, we examine the impact of the x and y dimensions on the phase diagram. In Fig. 3(a), we directly calculated the ground state IPR as a function of h for $V = 1$ at different sizes $L_x = 21, 34, 55, 89, 144, 233$. For L_x ranging from 21 to 233, there are respectively 2, 3, 4, 5, 8, and 13 critical points. With $L_x = 21$, the system has only two critical points, similar to what is shown in Fig. 1(b). This trend highlights that the number of discontinuities in the IPR scales with size changes.

Further analyses in Appendix A reveal that the discontinuities in the IPR correspond to changes in the derivation of ground state energy for $L_x = 21, 34, 55, 89$. The energy functions for general multiple imaginary domains, however, remain continuous. At these critical points, level crossing between ground and excited states suggests the occurrence of a FOQPT.

We make the first observation of the FOQPT induced by domain in non-Hermitian systems, characterized by the critical phase undergoing partitioning into multiple regions, which is a phenomenon absent in Hermitian systems. We thus define N_{QPT} as the number of FOQPTs induced by the quasicrystal imaginary domains.

We plot the N_{QPT} as a function of L_x/L_y , as shown in Fig. 3(b). The results show that N_{QPT} remains constant with increasing L_y , as indicated by the green line, due to the constant size of the quasicrystal domain ($V(x)$). However, the N_{QPT} increases as L_x increases, as represented by the red line. The linear fit result is $N_{QPT} = 0.05L_x + 0.98$. 0.05 means that for every 20 lattices, there is a phase transition increase in the imaginary potential. Notably, the observed increase phase transition is not the extended-critical or critical-localized

transition, but rather a FOQPT. Considering the potential $V(x)$ in Eq. (2), the emergence of zeros in the potential ($\text{Im}(V(x)) \approx 0$) is crucial. When we calculated the zero points of the quasicrystal domains for these sizes, we find an average of one zero point appearing every 20 lattice sites as well. That is, the number of quasicrystal domains equals (N_d) the number of FOQPTs (N_{QPT}). This correlation is further supported by the ground state fidelity analysis in Fig. 3(b) subplot. The fidelity of the ground state F_g as a function of h for different sizes $L_x = 21, 34, 55, 89, 144, 233$. As the L_x increases, the number of zero imaginary potential points increases. These zeros partition the potential into distinct domains, with each domain hosting different phase transition points as the h vary. This is the reason why the N_{QPT} increases as the L_x [length of the $V(x)$] increases.

Moreover, if these zeros are replaced by finite imaginary potentials, the N_{QPT} returns to the situation in Fig. 3(b) and does not vary with L_x , as illustrated by the green line. Additionally, when maintaining a constant length of the imaginary potential, i.e. $\text{length}(V(x)) = 20$, we plot the N_{QPT} as a function of L_x , as indicated by the green line. This implies that the first depends only on the changes in the imaginary domain.

Furthermore, based on the above discussion, imaginary domains not only induce FOQPT but also confine the ground state wave function within the domain regions with the lowest potential energy. However, as seen in Fig. 3(a), around the FOQPT, there is a slight discontinuity in the ground state probability. Additionally, with increasing size, the variation in this IPR becomes progressively smaller. We have computed the average of the differences in the IPR (IPR_δ) at all critical points as a function of L_x . Through log-log fitting, we find that $IPR_\delta \propto L_x^{-0.84}$, as shown in Fig. 3(c). Therefore, in the thermodynamic limit, the localization transition of the system from critical to localized phase would be a continuous one.

In Appendix D, we also discuss the relationship between the critical points h_1, h_2 , and the system dimensions L_x, L_y . We observe that only h_2 is influenced by L_x , showing an approximately linear growth with increasing L_x . This further indicates that the transition from the critical phase to the localized phase is expected to be a continuous process in the thermodynamic limit.

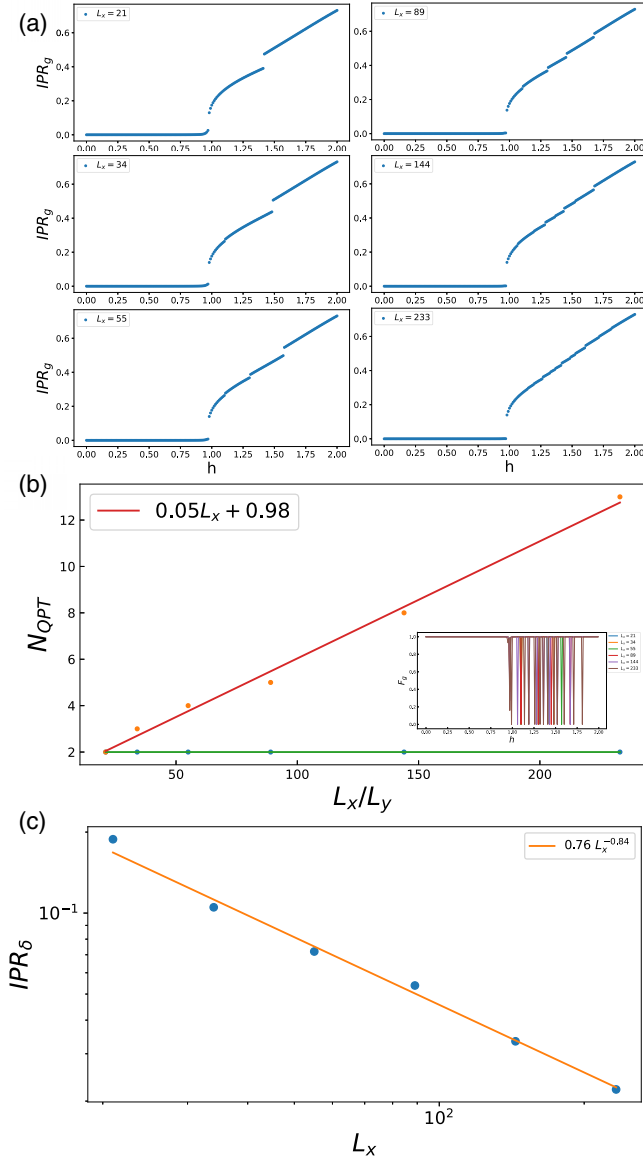


FIG. 3. (a) The IPR_g as a function of h for six different system sizes $L_x = 21, 34, 55, 89, 144, 233$. (b) The N_{QPT} as a function of L_x/L_y . The red line represents L_x , and the fit yields $N_{QPT} = 0.05L_x + 0.98$. The green line corresponds to L_y . Inset: The ground fidelity F_g plotted against h with $L_x = 21, 34, 55, 89, 144, 233$. (c) The average of difference in IPR (IPR_δ) at critical points as a function of L_x .

V. CONCLUSION

We have systematically explored the intricate phase diagram and the emergence of an FOQPT in the 2D Haldane model with edge quasicrystal dissipation. The system exhibits extended, critical, and localized phases, where the critical phase does not appear among the corresponding 1D AAH models. In the low-energy approximation, we show phase transitions in the density of the wave function within different phases.

Furthermore, the effect of the system dimensions along both x and y directions on these phase transitions has been also analyzed. While variations in the y direction dimensions exhibit no significant impact on the phase transitions,

increasing the dimensions along the x direction leads to a notable expansion of the critical point, marking the transition from the critical to the localized phase. This expansion can be attributed to the gain effect of the positive imaginary potential, which weakens the localization of the wave function. Moreover, our study unveils an interesting phenomenon in non-Hermitian systems: a FOQPT triggered by quasicrystal imaginary domains. This intriguing occurrence results in the critical phase partitioning into multiple regions as the size of the imaginary domain increases. Finally, these results deepen comprehension of the intricate interplay between the critical phase, edge quasicrystal domain, and system dimensions. These results also pave the way for further investigations into the realm of critical phases and quantum phase transitions.

ACKNOWLEDGMENTS

We are grateful to Yiling Zhang, Xue-Ping Ren, Xin-Ran Ma, Qian Du, Zheng Wei, Yufei Zhu, and Xin-Xin Yang for their valuable suggestions on the manuscript. This work is supported by NSFC Grants No. 11974053 and No. 12174030, as well as the National Key R&D Program of China (Grant No. 2023YFA1406704).

APPENDIX A: FIRST-ORDER PHASE TRANSITION

According to Landau's criterion, a quantum phase transition is identified by the non-analytic behavior of the ground state energy. This nonanalyticity can manifest as the limiting case of avoided level crossing or actual level crossing [79]. Furthermore, an n th-order quantum phase transition is characterized by discontinuities in the n th derivative of the energy [80]. However, the spectra of the non-Hermitian system are generally complex. There are some line gaps and point gaps that have been found in the non-Hermitian systems [6,71]. When the parameters are changed, the line gap may go through the process of closing and reopening many times if there is more than one zero imaginary potential point. Therefore, in our system, FOQPT is identified by abrupt changes in the real part of the energy gap Δ_g and the first derivative of the ground state energy dE_g/dh . In Fig. 4(a), we plot the logarithm of the energy gap $\log(\Delta_g)$ as a function of h for different system sizes $L_x = 21, 34, 55, 89$,

$$\Delta_g = \text{Re}(E_f - E_g), \quad (\text{A1})$$

where E_f is the first excited state energy and E_g is the ground state energy. There are two discontinuous points h_1 and h_2 , at which the gap is closed. It also corresponds to the phase transition at $V = 1$ in Fig. 1(b) in the main text.

To determine the order of a phase transition, we calculated the ground state energy E_g and its first derivative dE_g/dh as a function of h . In Fig. 4(b), the black dots represent the ground state energy, while the red dots represent its first derivative. Although E_g is continuous, the discontinuity of dE_g/dh at h_1 and h_2 , showing the first-order nature of quantum phase transition, as illustrated in Fig. 4(a).

For the Hamiltonian system described by Eq. (13) in the main text, we also investigated the phase transitions in a 1D nonadjacent imaginary domain system. As illustrated in Fig. 5, we computed the ground state energies and their derivatives for different system sizes ($L = 40, 60, 80, 100$).

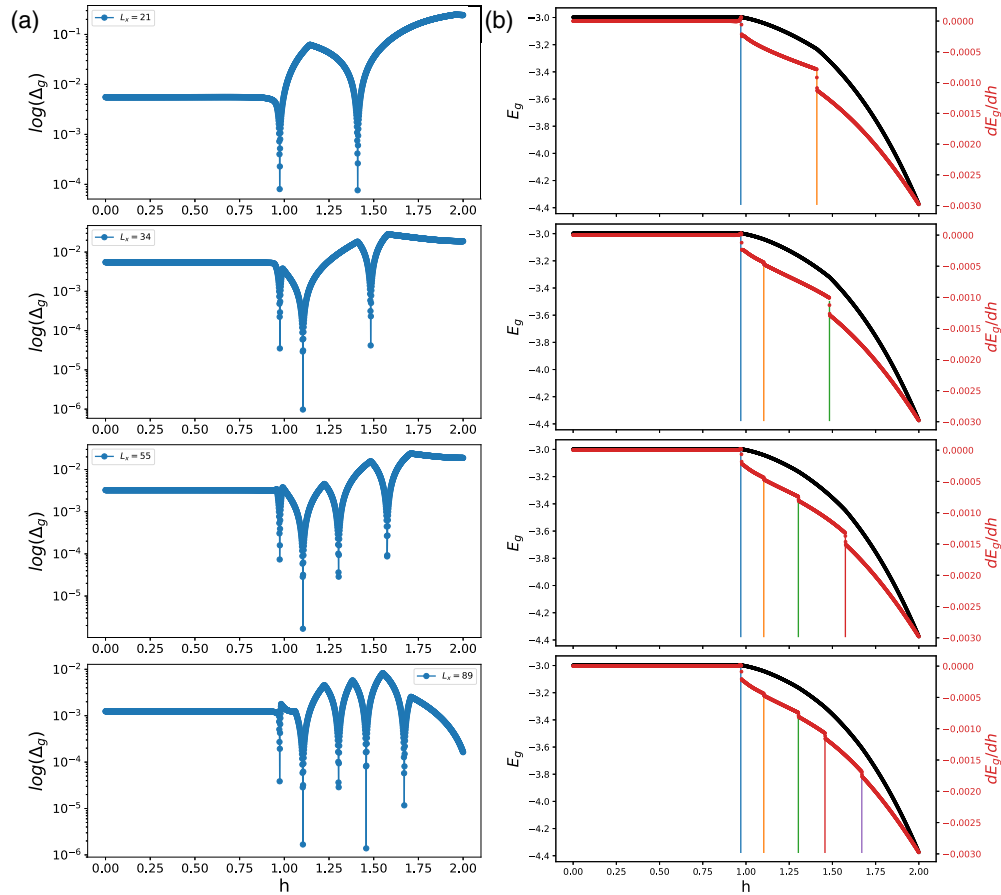


FIG. 4. (a) The logarithm of energy gap $\log(\Delta_g)$ as a function of h . (b) The first-order derivative of the ground state energy dE_g/dh as a function of h . Both $\log(\Delta_g)$ and dE_g/dh exhibit discontinuities for four different system sizes $L_x = 21, 34, 55, 89$. The parameters are chosen as $V = 1, L_y = 20$.

However, unlike the scenario depicted in Fig. 4, we did not observe any discontinuous changes indicative of phase transitions. Specifically, the parameter variations in a typical virtual domain system did not give rise to first-order quantum phase transitions or energy level crossings. This stands in contrast to the distinctive phenomenon observed in the 2D quasicrystal domain system, which represents a unique case in our research.

APPENDIX B: FRACTION DIMENSION, PT-SYMMETRY BREAKING, AND FIDELITY

The localization behavior of the system's wave function is a crucial observable that requires precise measurements. Wave functions are commonly characterized by their fractal dimension (FD) [54,66], quantified by the IPR, which follows a scaling relation of

$$\text{IPR} \sim (L_x)^{-\tau}, \quad (\text{B1})$$

where τ represents the FD. The FD provides a valuable perspective to understand how states expand and fluctuate as the system size increases. Similar to IPR, when $\lim_{L_x \rightarrow \infty} \tau = 1$, it indicates an extended wave function. Conversely, if the wave function is localized with peaks only at a few lattice points and negligible amplitudes elsewhere, it implies $\lim_{L_x \rightarrow \infty} \tau = 0$. Fractal wave functions exhibit FD values within the range of $0 < \lim_{L_x \rightarrow \infty} \tau < 1$.

In Figs. 6(a)–6(c), we compare the fractal dimensions of the extended, localized, and critical phases. Specifically, we examine three points along the $V = 1$ line in Fig. 1(b) of the main text: $h = 0.2, 1.4$, and 2.6 . The two black dashed lines in all plots correspond to $\text{Re}(E) = \pm 1$ positions, between which states are all topological edge states only when h is small. In Fig. 6(a) at $h = 0.2$, the majority of states are concentrated at the top, indicating extended states with $\tau = 1$. Moving to Fig. 6(b) with $h = 1.4$, a decreasing trend is observed in both topological edge states and boundary states, with τ values ranging from 0.1 to 0.6. These boundary states tend to localize at points on the imaginary lattice. Additionally, some of these states satisfy $|\text{Re}(E)| < 1$, indicating the occurrence of an energy level-crossing, i.e., a first-order phase transition. It is worth noting that at $\tau = 0.6$, we observe the separation between extended states and fractal states localized on the dissipative boundary.

Under a strong imaginary potential at $h = 2.6$ in Fig. 6(c), we discover that all boundary states move to the bottom with $\tau = 0$, and their count precisely matches the number of topological edge states L_x . However, the topological edge states return to the top of the plot, indicating their return to extended states almost unaffected by the imaginary potential.

The impact of the imaginary potential on the system's topological states is observed in the critical phase, as depicted in Figs. 6(b). A captivating question arises: How does the

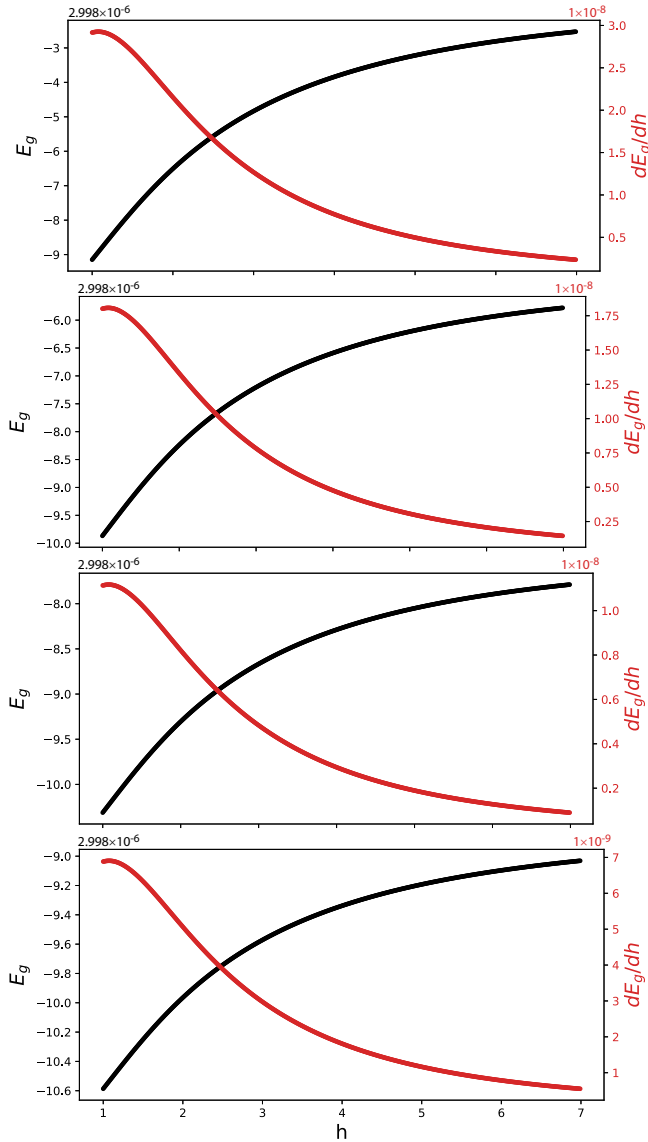


FIG. 5. The ground state energies (black points) and their derivatives (red points) for the Hamiltonian (Eq. 13) as a function of h at $L = 40, 60, 80,$ and 100 . The derivatives of the ground state energies did not exhibit any discontinuous changes.

variation of the parameter influence the imaginary part of the topological edge states? Figure 6(d) illustrates the behavior of the largest imaginary part $|\text{Im}(E)|$ vs h . Remarkably, a sudden surge from zero occurs at h_1 , followed by an abrupt decline to zero at h_2 . Remarkably, when $h < h_1$ (PT-symmetric) and $h > h_2$ (PT-restored), $\max(\text{Im}(E_e))$ remains close to zero, in agreement with Figs. 4(a) and 4(b). However, in the intermediate region, the imaginary potential has a pronounced impact on the topological states, leading to non-zero values of $\text{Im}(E_e)$. This observation verifies our earlier conjecture and highlights the intricate interplay between the parameter variation and the imaginary part of the topological edge states, see Eq. (6) of the main text.

One calculation similar to the FD is the scaling exponent [54,66], which can be obtained from the on-site probabilities of any wave function ψ_n . Specifically, the on-site probability

is restricted to the boundary. According to the fractal theorem, the scaling of the maximum on-site probability is expressed as

$$\max(p_{n,\text{edge}}) \sim (2L_x)^{-\beta_{\min}^{\text{edge}}}, \quad (\text{B2})$$

where $p_{n,\text{edge}} = |\psi_{n,\text{edge}}|^2$ and $\text{edge} = 1, \dots, 2L_x$. To determine the extended, critical, and localized wave functions, we only need to investigate the minimum value of the scaling exponent $\beta_{\min}^{\text{edge}}$.

Referring to Fig. 6(e), we focus on the scaling exponent of the ground state on the boundary. Strikingly, we observe a precipitous decline in $\beta_{\min}^{\text{edge}}$ precisely at the critical points h_1 and h_2 . When $h < h_1$, the system manifests an extended phase, thereby approximating $\beta_{\min}^{\text{edge}}$ to 1. Conversely, for $h > h_2$, the system assumes a localized phase, whereby the boundary wave functions localize, yielding $\beta_{\min}^{\text{edge}} \approx 0$. Within the critical phase, $\beta_{\min}^{\text{edge}}$ spans the interval $(0.1, 0.25)$, providing evidence of a fractal nature of the ground state.

We have carried out various calculations, some of which are based on knowledge of the physical properties of the system. However, in Fig. 6(f), we investigate the behavior of the ground state fidelity F_g vs h [81]. Fidelity has a distinct advantage in that it does not require prior familiarity with the order parameters or symmetries of the system. Typically, we can expect that as the ground-state structure undergoes sharp changes, the fidelity will abruptly decrease near the critical points of the system. We focus on the boundary subspace and explore the boundary fidelity, quantified as

$$F_g(h, \delta h) = |\langle \psi_{g,\text{edge}}(h) | \psi_{g,\text{edge}}(h + \delta h) \rangle|, \quad (\text{B3})$$

where δh is a small quantity, $|\psi_{g,\text{edge}}(h)\rangle = \sum_{\text{edge}} |\psi_{\text{edge}}\rangle \langle \psi_{\text{edge}} | \psi_g(h)\rangle$ and $|\psi_g(h)\rangle$ satisfies the eigenvalue equation $H(h) |\psi_g(h)\rangle = E_g |\psi_g(h)\rangle$. Around the critical points near h_1 and h_2 , the overlap of the ground state F_g undergoes a dramatic decrease, decreasing from 1 to 0.76 and from 1 to 0, respectively.

Based on the above description, the physical properties of the original Haldane model can essentially be captured by the characteristics of its boundaries. Therefore, we introduce the concept of the boundary effective Hamiltonian H_{edge} to further comprehend the expanded-critical and critical-localized phase transitions depicted in Fig. 1(b) in the main text. Directly, we project the H onto the boundary subspace by using the boundary projection operator P_{edge} . The effective edge Hamiltonian is then given by

$$H_{\text{eff}} = P_{\text{edge}} H P_{\text{edge}} = H_{\text{AA}} + H_{\text{free}} + H_c, \quad (\text{B4})$$

where $H_{\text{AA}} = \sum_m (a_m^\dagger a_{m+1} + \text{H.c.}) + V \cos(2\pi\alpha m + ih) a_m^\dagger a_m$ represents the non-Hermitian Aubry-André-Harper model, $H_{\text{free}} = \sum_m b_{m+1}^\dagger b_m + \text{H.c.}$ is the free chain with only the nearest-neighbor hopping term, and $H_c = a_m^\dagger b_m + \text{H.c.}$ represents their coupling, as seen in Eq. (1) of the main text with $L_y = 2$. The H_{eff} is reduced to a two-chain model

$$H_{\text{eff}} = \sum_{j=1}^2 \sum_n [V_{j,m} c_{j,m}^\dagger c_{j,m} + t(c_{j,m}^\dagger c_{j,m+1} + \text{H.c.})] + \lambda \sum_{m=\text{odd}} (c_{1,m}^\dagger c_{2,m} + \text{H.c.}), \quad (\text{B5})$$

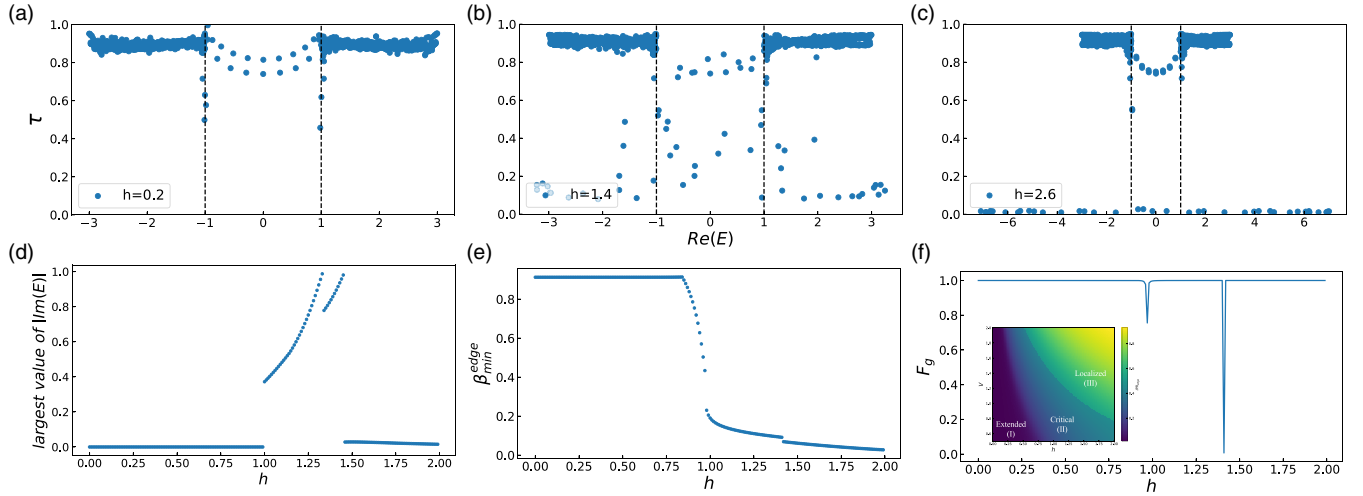


FIG. 6. [(a)–(c)]. The fractal dimensions τ as a function of the real part of eigenenergies $Re(E)$ for three different $h = 0.2, 1.4, 2.6$. In (d), the largest value of $|Im(E)|$ is a function of h . (e) The minimal scaling exponent as a function of h . (f) The fidelity of ground states F_g versus h . Abrupt changes at h_1 and h_2 are present in [(d)–(f)]. Inset: Phase diagram of the effective two-chain model H_{eff} . The parameters are chosen as $L_x = 20, L_y = 20$.

where $V_{1,m} = V \cos(2\pi\alpha m + ih)$ when $j = 1$ and when $j = 2, V_{2,m} = 0$.

In the subplot of Fig. 6(f), two critical lines, similar to those in Fig. 1(b) of the main text, divide the whole phase diagram into three regions: extended, localized, and critical phases. This phase diagram is almost the same as Fig. 1(c) in the main text, except that the critical line from the extended phase to the critical phase is not particularly obvious, and the extended phase is also reduced. This is due to size effects, and in the case of $L_y \rightarrow \infty$ the subplot of Fig. 6(f) will change back to Fig. 1(b) in the main text.

APPENDIX C: PHASE TRANSITION IN IMAGINARY POTENTIAL

Now we replace H_h in Eqs. (12) and (13) of the main text by a 4×4 PT-symmetric matrix. This matrix is represented by four lattice models with different imaginary potentials. In the first case, two nonadjacent lattices feature dissipative behavior, while the other two do not. The corresponding Hamiltonian is denoted as $H_{NNN} = H_a$

$$H_a = \begin{pmatrix} i\gamma & t & 0 & 0 \\ t & 0 & t & 0 \\ 0 & t & i\gamma & t \\ 0 & 0 & t & 0 \end{pmatrix}, \quad (C1)$$

where the t is the nearest hopping term and the γ is the non-adjacent on-site imaginary potential. H_a is PT-symmetric, i.e., $PTH_a(P)^\dagger = H_a$. The exceptional points are $\gamma = (\sqrt{5} \pm 1)t$, and the eigenvalues are

$$\begin{aligned} \lambda_1 &= \frac{1}{2}(-\sqrt{-\gamma^2 - 2(\sqrt{5}-3)t^2} + i\gamma), \\ \lambda_2 &= \frac{1}{2}(\sqrt{-\gamma^2 - 2(\sqrt{5}-3)t^2} + i\gamma), \\ \lambda_3 &= \frac{1}{2}(-\sqrt{2(\sqrt{5}+3)t^2 - \gamma^2} + i\gamma), \\ \lambda_4 &= \frac{1}{2}(\sqrt{2(\sqrt{5}+3)t^2 - \gamma^2} + i\gamma). \end{aligned} \quad (C2)$$

As the eigenvalues are symmetric, we only need to consider $\gamma > 0$, see Fig. 7(a). The system holds PT symmetry when $\gamma < (\sqrt{5}-1)t$, where $Im(\lambda_1, \lambda_2)$ are all equal to each other. When $(\sqrt{5}-1)t < \gamma < (\sqrt{5}+1)t$, the imaginary part $Im(\lambda_1, \lambda_2)$ are different, so $\gamma = \gamma_{c1} = (\sqrt{5}-1)t$ is the first critical point. Moreover, when γ exceeds the second critical point $\gamma = \gamma_{c2} = (\sqrt{5}+1)t$, the vanishing of the real part of the four modes indicates that PT-symmetry is broken again.

Conversely, the Hamiltonian with two adjacent imaginary potentials is

$$H_b = \begin{pmatrix} i\gamma & t & 0 & 0 \\ t & i\gamma & t & 0 \\ 0 & t & 0 & t \\ 0 & 0 & t & 0 \end{pmatrix}, \quad (C3)$$

where H_b is also PT-symmetric. Then the eigenvalues of H_b are

$$\begin{aligned} \lambda_1 &= \frac{1}{2}(-\sqrt{-\gamma^2 - 2t\sqrt{5t^2 - 4\gamma^2} + 6t^2} + i\gamma), \\ \lambda_2 &= \frac{1}{2}(\sqrt{-\gamma^2 - 2t\sqrt{5t^2 - 4\gamma^2} + 6t^2} + i\gamma), \\ \lambda_3 &= \frac{1}{2}(-\sqrt{-\gamma^2 + 2t\sqrt{5t^2 - 4\gamma^2} + 6t^2} + i\gamma), \\ \lambda_4 &= \frac{1}{2}(\sqrt{-\gamma^2 + 2t\sqrt{5t^2 - 4\gamma^2} + 6t^2} + i\gamma). \end{aligned} \quad (C4)$$

However, there is only one exceptional point $\gamma = \gamma_{c1} \approx 1.1$ where $Im(\lambda_1) = Im(\lambda_2)$ and $Im(\lambda_3) = Im(\lambda_4)$, as shown in Fig. 7(b). As in Eq. (13) of the main text, the Hamiltonian of a 1D free chain with different imaginary domain walls is given by

$$H_{NN} = H_{\text{Hermitian}} + iV_1 + iV_2/4, \quad V_1 = V_2, \quad (C5)$$

where H_{NN} represent the nearest-neighbor imaginary domain. $H_{\text{Hermitian}} = \sum_n c_n^\dagger c_n + \text{H.c.}$ is a free chain. $V_1 = V \sum_{n=1}^{L_x/4} x_n$, $V_2 = V \sum_{n=3L_x/4}^{L_x} x_n$ are the first and second domains

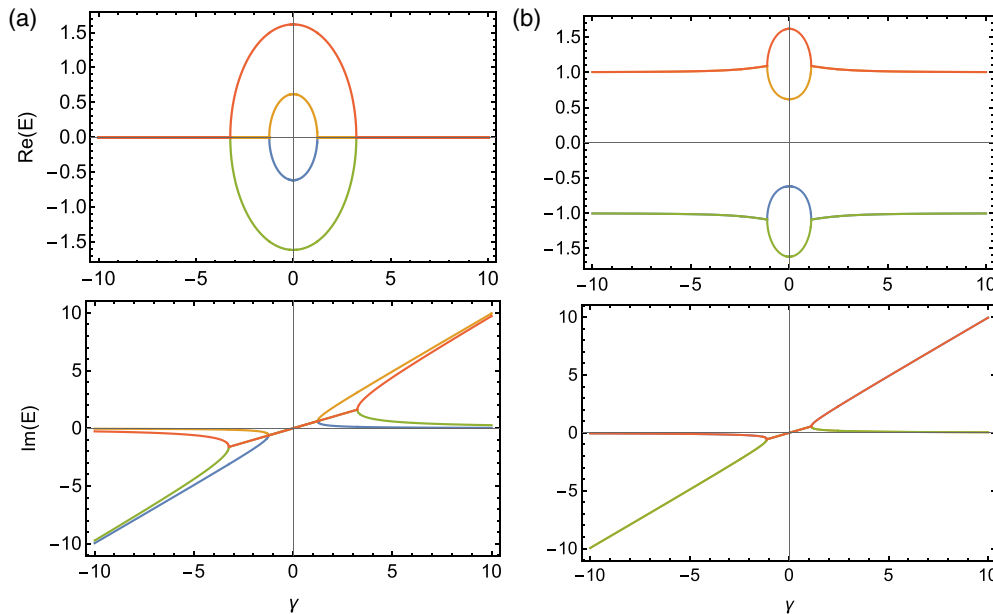


FIG. 7. The energy spectrum of the simplest four lattice model. (a) The real and imaginary parts of the energy spectrum of H_a as a function of γ . (b) The real and imaginary parts of the energy spectrum of H_b as a function of γ .

respectively, and V is the strength of imaginary domain.

$$H_{NNN} = H_{\text{Hermitian}} + iV_1 + iV_3/4, \quad V_1 = V_2 \quad (\text{C6})$$

where H_{NNN} represent the next-nearest-neighbor imaginary domain. $V_1 = V \sum_{n=1}^{\frac{L_x}{2}} x_n$, $V_3 = V \sum_{n=\frac{L_x}{2}}^{L_x} x_n$ are the first and second domains respectively, and V is the strength of imaginary domain.

In Eq. (13) of the main text, we have the Hamiltonian for a one-dimensional free chain with distinct imaginary domain walls. Examining Fig. 8(a), for nonadjacent imaginary domains, the complex spectrum initially approximates a straight line. As the strength of the domains increases, a PT phase transition occurs, leading to the emergence of a line gap. Upon further increasing the strength of the imaginary domains, another line gap appears, indicating another PT phase transition. In other words, two nonadjacent imaginary domains induce two PT phase transitions. However, the adjacent domain undergoes only one PT phase transition with the variation of parameter V , see Fig. 8(b). This conclusion further corroborates the scenario discussed in Fig. 3(b) of the main text. In the following, we aim to figure out the connection between the 2D Haldane model and the imaginary potential. Figure 9 illustrates the complex energy spectrum of two scenarios: one with NN imaginary potential [Fig. 9(a)], defined as

$$H_{NN} = H_{\text{Hermitian}} + iV_1 + iV_2/2, \quad V_1 = V_2, \quad (\text{C7})$$

and another with NNN imaginary potential [Fig. 9(b)] given by

$$H_{NNN} = H_{\text{Hermitian}} + iV_1 + iV_3/2, \quad V_1 = V_3, \quad (\text{C8})$$

where $H_{\text{Hermitian}}$ is an arbitrary Hermitian matrix, we consider the 2D Haldane model $H_{\text{Hermitian}} = H_{\text{Haldane}}$, see Eq. (3). In V_i ,

“ $i = 1, 2, 3$ ” represent the on-site potential of any position on the boundary and are increasing in order.

Their energy spectra form a semicircle with the x axis, exhibiting a skinning effect at $V = 1.600$, as shown in Fig. 9(a). The states close to the x -axis depict topological edge states influenced by the NN imaginary potentials. The two points with the largest imaginary part correspond to two boundary states, which are progressively confined towards the boundary due to the impact of the imaginary potential. The colors in Figs. 9(a) and 9(b) represent the density at the boundary $|\psi_{\text{edge}}|^2$, revealing that the topological edge states primarily occupy the boundary, while the states outside the energy gap are bulk states, except for the boundary states. At $V = V_c = 3.356$, a critical phase transition occurs when the two boundary states degenerate. If the imaginary potential is slightly larger, i.e., $V = 3.500$, the real part of these two states remains the same, but the imaginary part differs, resulting in a PT phase transition. With further increases in V , the energy of the boundary states increases in tandem with the imaginary potential, and the imaginary parts of the topological edge states become nearly zero, restoring PT symmetry.

We also consider the case of next-nearest-neighbor imaginary potentials for $V = 1.600, 2.000, 3.400, 6.000$. The energy spectra are more or less the same at the beginning, and the energy of the two boundary states undergoes a degenerate at $V = V_{c1} = 2.000$, which is also the first critical point. However, when $V = V_{c2} = 3.400$, two additional boundary states emerge near the topological edge states. These two boundary states undergo a second PT phase transition. After the occurrence of twice PT phase transitions, there are only boundary states localized at the two imaginary potential points, as shown in Fig. 9(b). This observation from the simplest case of two imaginary potentials can be extended to scenarios involving multiple imaginary potentials, where multiple PT phase transitions occur whenever nonadjacent imaginary

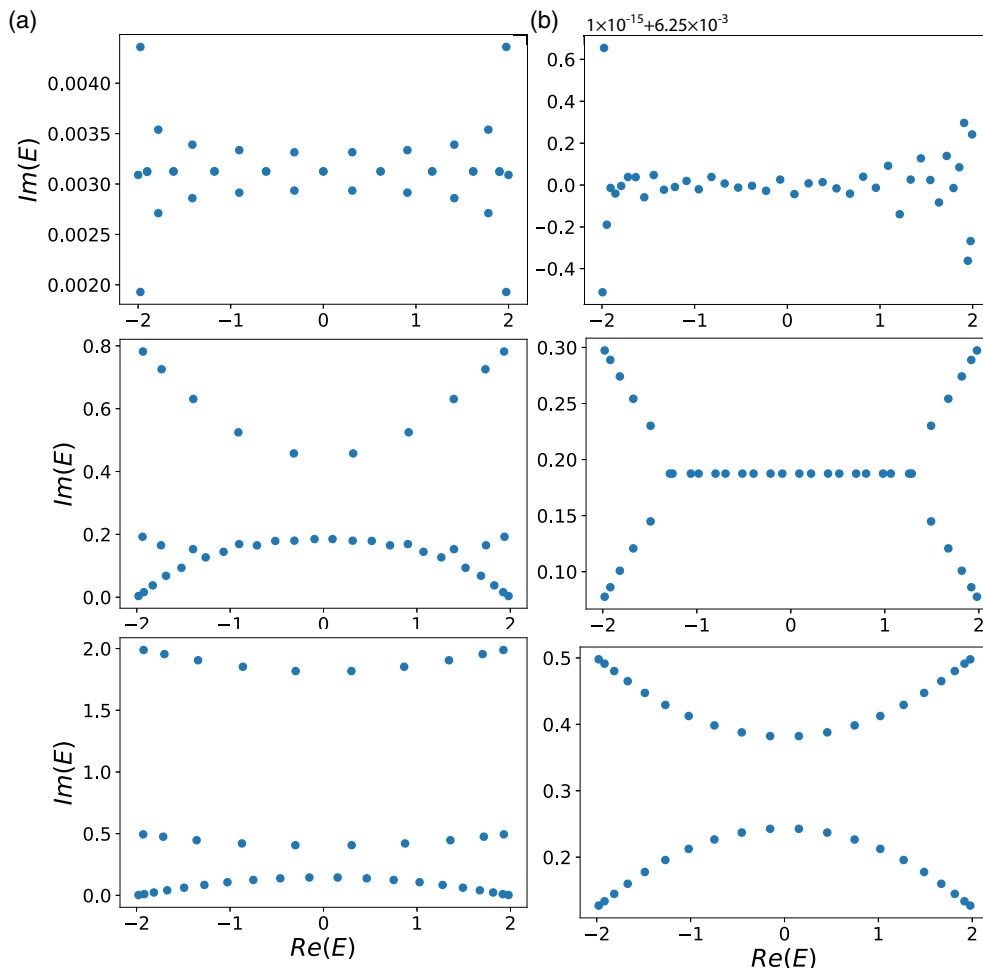


FIG. 8. The complex energy spectrum of the 1D free model with different imaginary impurities. (a) The energy spectra with two nonadjacent imaginary impurities for $V = 0.01, 0.80, 2.00$ from left to right. (b) The energy spectra with two adjacent imaginary impurities for $V = 0.01, 0.30, 0.50$ from left to right. The parameters are chosen as $L_x = 40$.

potentials are present, see Fig. 3(c). These nonadjacent imaginary potential points essentially act as domain walls separated by zeros. Consequently, as the size of the quasicrystal potential increases, FOQPT will be triggered continuously.

APPENDIX D: CRITICAL POINTS h_1 AND h_2

Not only the N_{QPT} are influenced by the dimensions L_x and L_y , but also the extended-critical transition point ($h - 1$) and the critical-localized transition point (h_2). The $\log(L_x)$ as

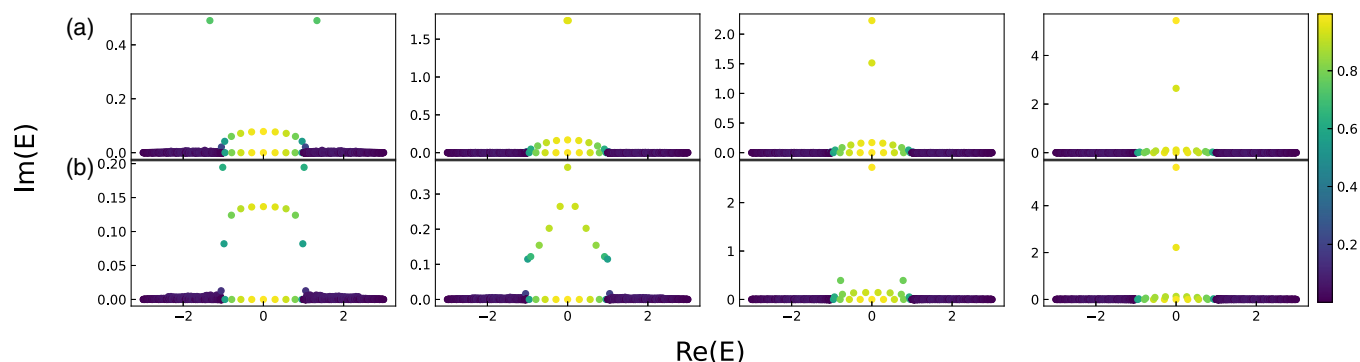


FIG. 9. The energy spectrum of the Haldane model with different imaginary impurities. (a) The energy spectra with two NN imaginary impurities for $V = 1.600, 3.356, 3.500, 6.000$ from left to right. (b) The energy spectra with two NNN imaginary impurities for $V = 1.600, 2.000, 3.400, 6.000$ from left to right. The parameters are chosen as $L_x = 20, L_y = 20$.

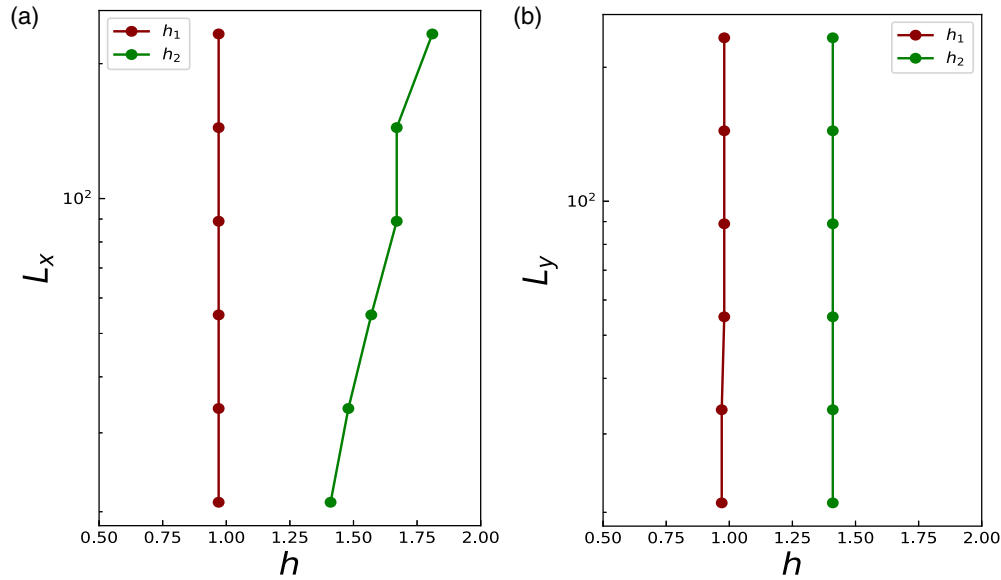


FIG. 10. (a) The x direction dimension L_x as a function of h_1/h_2 . (b) The y direction dimension L_y as a function of h_1/h_2 .

a function of h_1, h_2 is shown in Fig. 10(a), where we can see $h_1 \approx 0.97$ is almost a constant and $\log(L_x) = kh_2 + c$ is a linear function, where k and c are constants. As the size of the system increases, the alternation of positive and negative imaginary potentials becomes more pronounced. The presence of positive imaginary potentials causes the wave function [Eq. (8)] to spread towards regions marked by such potentials. This inherent tendency results in the wave functions localization transition points increasing as the system dimensions (L_x) grow. And each PT phase transition leads

to a more localized wave function. Thus, when combined with the calculations for IPR_δ in the main text, the critical phase undergoes a continuous transition to the localized phase in the thermodynamic limit. Moreover, h_1, h_2 is shown in Fig. 10(b) as L_y varies, when h_1, h_2 are all essentially constants.

It is important to note that, in the case of small system sizes, the critical points h_1 and h_2 are affected by the parameter L_y . Only when L_y is relatively large (with $L_y \geq 20$) do these two critical points tend to stabilize as constants.

-
- [1] H. J. Carmichael, Quantum trajectory theory for cascaded open systems, *Phys. Rev. Lett.* **70**, 2273 (1993).
- [2] C. M. Bender, Making sense of non-Hermitian Hamiltonians, *Rep. Prog. Phys.* **70**, 947 (2007).
- [3] R. El-Ganainy, K. G. Makris, M. Khajavikhan, Z. H. Musslimani, S. Rotter, and D. N. Christodoulides, Non-Hermitian physics and PT symmetry, *Nat. Phys.* **14**, 11 (2018).
- [4] C. M. Bender and S. Boettcher, Real spectra in non-Hermitian Hamiltonians having \mathcal{PT} symmetry, *Phys. Rev. Lett.* **80**, 5243 (1998).
- [5] M.-A. Miri and A. Alù, Exceptional points in optics and photonics, *Science* **363**, eaar7709 (2019).
- [6] Y. Ashida, Z. Gong, and M. Ueda, Non-Hermitian physics, *Adv. Phys.* **69**, 249 (2020).
- [7] S. Yao and Z. Wang, Edge states and topological invariants of non-Hermitian systems, *Phys. Rev. Lett.* **121**, 086803 (2018).
- [8] K. Kawabata, K. Shiozaki, M. Ueda, and M. Sato, Symmetry and topology in non-Hermitian physics, *Phys. Rev. X* **9**, 041015 (2019).
- [9] H. Zhou and J. Y. Lee, Periodic table for topological bands with non-Hermitian symmetries, *Phys. Rev. B* **99**, 235112 (2019).
- [10] A. Ghatak and T. Das, New topological invariants in non-Hermitian systems, *J. Phys.: Condens. Matter* **31**, 263001 (2019).
- [11] S. Yao, F. Song, and Z. Wang, Non-hermitian chern bands, *Phys. Rev. Lett.* **121**, 136802 (2018).
- [12] M. Kunitski, N. Eicke, P. Huber, J. Köhler, S. Zeller, J. Voigtsberger, N. Schlott, K. Henrichs, H. Sann, F. Trinter, L. P. H. Schmidt, A. Kalinin, M. S. Schöffler, T. Jahnke, M. Lein, and R. Dörner, Double-slit photoelectron interference in strong-field ionization of the neon dimer, *Nat. Commun.* **10**, 1 (2019).
- [13] V. M. Martinez Alvarez, J. E. Barrios Vargas, and L. E. F. Foa Torres, Non-Hermitian robust edge states in one dimension: Anomalous localization and eigenspace condensation at exceptional points, *Phys. Rev. B* **97**, 121401 (2018).
- [14] K. Yokomizo and S. Murakami, Non-bloch band theory of non-Hermitian systems, *Phys. Rev. Lett.* **123**, 066404 (2019).
- [15] C. H. Lee and R. Thomale, Anatomy of skin modes and topology in non-Hermitian systems, *Phys. Rev. B* **99**, 201103(R) (2019).
- [16] F. K. Kunst, E. Edvardsson, J. C. Budich, and E. J. Bergholtz, Biorthogonal bulk-boundary correspondence in non-Hermitian systems, *Phys. Rev. Lett.* **121**, 026808 (2018).
- [17] D. S. Borgnia, A. J. Kruchkov, and R.-J. Slager, Non-Hermitian boundary modes and topology, *Phys. Rev. Lett.* **124**, 056802 (2020).
- [18] A. McDonald, T. Pereg-Barnea, and A. A. Clerk, Phase-dependent chiral transport and effective non-Hermitian

- dynamics in a bosonic Kitaev-Majorana chain, *Phys. Rev. X* **8**, 041031 (2018).
- [19] K. Zhang, Z. Yang, and C. Fang, Correspondence between winding numbers and skin modes in non-Hermitian systems, *Phys. Rev. Lett.* **125**, 126402 (2020).
- [20] S. Longhi, Probing non-Hermitian skin effect and non-bloch phase transitions, *Phys. Rev. Res.* **1**, 023013 (2019).
- [21] L. Li, C. H. Lee, S. Mu, and J. Gong, Critical non-Hermitian skin effect, *Nat. Commun.* **11**, 5491 (2020).
- [22] W. Song, W. Sun, C. Chen, Q. Song, S. Xiao, S. Zhu, and T. Li, Breakup and recovery of topological zero modes in finite non-Hermitian optical lattices, *Phys. Rev. Lett.* **123**, 165701 (2019).
- [23] H. Zhao, X. Qiao, T. Wu, B. Midya, S. Longhi, and L. Feng, Non-Hermitian topological light steering, *Science* **365**, 1163 (2019).
- [24] S. Weidemann, M. Kremer, T. Helbig, T. Hofmann, A. Stegmaier, M. Greiter, R. Thomale, and A. Szameit, Topological funneling of light, *Science* **368**, 311 (2020).
- [25] B. Hu, Z. Zhang, H. Zhang, L. Zheng, W. Xiong, Z. Yue, X. Wang, J. Xu, Y. Cheng, X. Liu, and J. Christensen, Non-Hermitian topological whispering gallery, *Nature (London)* **597**, 655 (2021).
- [26] F. E. Ā-ztürk, T. Lappe, G. Hellmann, J. Schmitt, J. Klaers, F. Vewinger, J. Kroha, and M. Weitz, Observation of a non-Hermitian phase transition in an optical quantum gas, *Science* **372**, 88 (2021).
- [27] K. Wang, A. Dutt, K. Y. Yang, C. C. Wojcik, J. Vukovi, and S. Fan, Generating arbitrary topological windings of a non-Hermitian band, *Science* **371**, 1240 (2021).
- [28] L. Xiao, T. Deng, K. Wang, Z. Wang, W. Yi, and P. Xue, Observation of non-Bloch parity-time symmetry and exceptional points, *Phys. Rev. Lett.* **126**, 230402 (2021).
- [29] Q. Lin, T. Li, L. Xiao, K. Wang, W. Yi, and P. Xue, Topological phase transitions and mobility edges in non-Hermitian quasicrystals, *Phys. Rev. Lett.* **129**, 113601 (2022).
- [30] C. H. Lee, L. Li, and J. Gong, Hybrid higher-order skin-topological modes in nonreciprocal systems, *Phys. Rev. Lett.* **123**, 016805 (2019).
- [31] K. Kawabata, M. Sato, and K. Shiozaki, Higher-order non-Hermitian skin effect, *Phys. Rev. B* **102**, 205118 (2020).
- [32] Y. Li, C. Liang, C. Wang, C. Lu, and Y.-C. Liu, Gain-loss-induced hybrid skin-topological effect, *Phys. Rev. Lett.* **128**, 223903 (2022).
- [33] X. Ma, K. Cao, X. Wang, Z. Wei, and S. Kou, Non-Hermitian chiral skin effect, *Phys. Rev. Res.* **6**, 013213 (2024).
- [34] F. Yang, X.-P. Ren, and S. peng Kou, Non-Hermitian chiral edge modes with complex fermi velocity, [arXiv:2307.14144](https://arxiv.org/abs/2307.14144) [cond-mat.str-el].
- [35] Q. Du, X.-R. Ma, and S.-P. Kou, Non-Hermitian tearing by dissipation, [arXiv:2307.14340](https://arxiv.org/abs/2307.14340) [cond-mat.mes-hall].
- [36] P. G. Harper, Single band motion of conduction electrons in a uniform magnetic field, *Proc. Phys. Soc. A* **68**, 874 (1955).
- [37] S. Aubry and G. André, Analyticity breaking and Anderson localization in incommensurate lattices, *Ann. Israel Phys. Soc.* **3**, 18 (1980).
- [38] G. Jotzu, M. Messer, R. Desbuquois, M. Lebrat, T. Uehlinger, D. Greif, and T. Esslinger, Experimental realization of the topological Haldane model with ultracold fermions, *Nature (London)* **515**, 237 (2014).
- [39] G. Roati, C. D'Errico, L. Fallani, M. Fattori, C. Fort, M. Zaccanti, G. Modugno, M. Modugno, and M. Inguscio, Anderson localization of a non-interacting Bose-Einstein condensate, *Nature (London)* **453**, 895 (2008).
- [40] Y. Lahini, R. Pugatch, F. Pozzi, M. Sorel, R. Morandotti, N. Davidson, and Y. Silberberg, Observation of a localization transition in quasiperiodic photonic lattices, *Phys. Rev. Lett.* **103**, 013901 (2009).
- [41] Y. E. Kraus, Y. Lahini, Z. Ringel, M. Verbin, and O. Zilberberg, Topological states and adiabatic pumping in quasicrystals, *Phys. Rev. Lett.* **109**, 106402 (2012).
- [42] L.-J. Lang, X. Cai, and S. Chen, Edge states and topological phases in one-dimensional optical superlattices, *Phys. Rev. Lett.* **108**, 220401 (2012).
- [43] S. Ganeshan, K. Sun, and S. Das Sarma, Topological zero-energy modes in gapless commensurate Aubry-André-Harper models, *Phys. Rev. Lett.* **110**, 180403 (2013).
- [44] M. Verbin, O. Zilberberg, Y. E. Kraus, Y. Lahini, and Y. Silberberg, Observation of topological phase transitions in photonic quasicrystals, *Phys. Rev. Lett.* **110**, 076403 (2013).
- [45] J. Sokoloff, Unusual band structure, wave functions and electrical conductance in crystals with incommensurate periodic potentials, *Phys. Rep.* **126**, 189 (1985).
- [46] S. Longhi, Phase transitions in a non-Hermitian Aubry-André-Harper model, *Phys. Rev. B* **103**, 054203 (2021).
- [47] A. P. Acharya, A. Chakrabarty, D. K. Sahu, and S. Datta, Localization, \mathcal{PT} symmetry breaking, and topological transitions in non-Hermitian quasicrystals, *Phys. Rev. B* **105**, 014202 (2022).
- [48] H. Hiramoto and S. Abe, Dynamics of an electron in quasiperiodic systems. II. Harper's model, *J. Phys. Soc. Jpn.* **57**, 1365 (1988).
- [49] R. Ketzmerick, K. Kruse, S. Kraut, and T. Geisel, What determines the spreading of a wave packet? *Phys. Rev. Lett.* **79**, 1959 (1997).
- [50] M. Larcher, F. Dalfovo, and M. Modugno, Effects of interaction on the diffusion of atomic matter waves in one-dimensional quasiperiodic potentials, *Phys. Rev. A* **80**, 053606 (2009).
- [51] T. Geisel, R. Ketzmerick, and G. Petschel, New class of level statistics in quantum systems with unbounded diffusion, *Phys. Rev. Lett.* **66**, 1651 (1991).
- [52] K. Machida and M. Fujita, Quantum energy spectra and one-dimensional quasiperiodic systems, *Phys. Rev. B* **34**, 7367 (1986).
- [53] C. L. Bertrand and A. M. García-García, Anomalous Thouless energy and critical statistics on the metallic side of the many-body localization transition, *Phys. Rev. B* **94**, 144201 (2016).
- [54] X. Lin, X. Chen, G.-C. Guo, and M. Gong, General approach to the critical phase with coupled quasiperiodic chains, *Phys. Rev. B* **108**, 174206 (2023).
- [55] T. C. Halsey, M. H. Jensen, L. P. Kadanoff, I. Procaccia, and B. I. Shraiman, Fractal measures and their singularities: The characterization of strange sets, *Phys. Rev. A* **33**, 1141 (1986).
- [56] A. D. Mirlin, Y. V. Fyodorov, A. Mildenerger, and F. Evers, Exact relations between multifractal exponents at the anderson transition, *Phys. Rev. Lett.* **97**, 046803 (2006).
- [57] R. Dubertrand, I. García-Mata, B. Georgeot, O. Giraud, G. Lemarié, and J. Martin, Two scenarios for quantum multifractality breakdown, *Phys. Rev. Lett.* **112**, 234101 (2014).

- [58] J. Wang, X.-J. Liu, G. Xianlong, and H. Hu, Phase diagram of a non-Abelian Aubry-André-Harper model with p -wave superfluidity, *Phys. Rev. B* **93**, 104504 (2016).
- [59] Y. Hatsugai and M. Kohmoto, Energy spectrum and the quantum hall effect on the square lattice with next-nearest-neighbor hopping, *Phys. Rev. B* **42**, 8282 (1990).
- [60] Y. Takada, K. Ino, and M. Yamanaka, Statistics of spectra for critical quantum chaos in one-dimensional quasiperiodic systems, *Phys. Rev. E* **70**, 066203 (2004).
- [61] F. Liu, S. Ghosh, and Y. D. Chong, Localization and adiabatic pumping in a generalized Aubry-André-Harper model, *Phys. Rev. B* **91**, 014108 (2015).
- [62] J. H. Han, D. J. Thouless, H. Hiramoto, and M. Kohmoto, Critical and bicritical properties of Harper's equation with next-nearest-neighbor coupling, *Phys. Rev. B* **50**, 11365 (1994).
- [63] Y. Wang, L. Zhang, S. Niu, D. Yu, and X.-J. Liu, Realization and detection of nonergodic critical phases in an optical raman lattice, *Phys. Rev. Lett.* **125**, 073204 (2020).
- [64] Y. Wang, C. Cheng, X.-J. Liu, and D. Yu, Many-body critical phase: Extended and nonthermal, *Phys. Rev. Lett.* **126**, 080602 (2021).
- [65] T. Xiao, D. Xie, Z. Dong, T. Chen, W. Yi, and B. Yan, Observation of topological phase with critical localization in a quasi-periodic lattice, *Sci. Bull.* **66**, 2175 (2021).
- [66] T. Liu, S. Cheng, H. Guo, and G. Xianlong, Fate of majorana zero modes, exact location of critical states, and unconventional real-complex transition in non-Hermitian quasiperiodic lattices, *Phys. Rev. B* **103**, 104203 (2021).
- [67] D. A. Abanin, E. Altman, I. Bloch, and M. Serbyn, Colloquium: Many-body localization, thermalization, and entanglement, *Rev. Mod. Phys.* **91**, 021001 (2019).
- [68] M. Schreiber, S. S. Hodgman, P. Bordia, H. P. Lüschen, M. H. Fischer, R. Vosk, E. Altman, U. Schneider, and I. Bloch, Observation of many-body localization of interacting fermions in a quasirandom optical lattice, *Science* **349**, 842 (2015).
- [69] M. Rispoli, A. Lukin, R. Schittko, S. Kim, M. E. Tai, J. Léonard, and M. Greiner, Quantum critical behaviour at the many-body localization transition, *Nature (London)* **573**, 385 (2019).
- [70] H. Jiang, L.-J. Lang, C. Yang, S.-L. Zhu, and S. Chen, Interplay of non-Hermitian skin effects and Anderson localization in nonreciprocal quasiperiodic lattices, *Phys. Rev. B* **100**, 054301 (2019).
- [71] S. Longhi, Topological phase transition in non-Hermitian quasicrystals, *Phys. Rev. Lett.* **122**, 237601 (2019).
- [72] Y. Wang, Y. Ke, Y.-J. Chang, Y.-H. Lu, J. Gao, C. Lee, and X.-M. Jin, Constructing higher-order topological states in higher dimensions, *Phys. Rev. B* **104**, 224303 (2021).
- [73] J.-J. Liu, Z.-W. Li, Z.-G. Chen, W. Tang, A. Chen, B. Liang, G. Ma, and J.-C. Cheng, Experimental realization of Weyl exceptional rings in a synthetic three-dimensional non-Hermitian phononic crystal, *Phys. Rev. Lett.* **129**, 084301 (2022).
- [74] S. Cheng, R. Asgari, and G. Xianlong, From topological phase to transverse anderson localization in a two-dimensional quasiperiodic system, *Phys. Rev. B* **108**, 024204 (2023).
- [75] A. G. Gavriluk, V. V. Struzhkin, A. G. Ivanova, V. B. Prakapenka, A. A. Mironovich, S. N. Aksenov, I. A. Troyan, and W. Morgenroth, The first-order structural transition in nio at high pressure, *Commun. Phys.* **6**, 23 (2023).
- [76] L. Liu, X. Lu, Y. Chu, G. Yang, Y. Yuan, F. Wu, Y. Ji, J. Tian, K. Watanabe, T. Taniguchi, L. Du, D. Shi, J. Liu, J. Shen, L. Lu, W. Yang, and G. Zhang, Observation of first-order quantum phase transitions and ferromagnetism in twisted double bilayer graphene, *Phys. Rev. X* **13**, 031015 (2023).
- [77] H. Cai, J. Liu, J. Wu, Y. He, S.-Y. Zhu, J.-X. Zhang, and D.-W. Wang, Experimental observation of momentum-space chiral edge currents in room-temperature atoms, *Phys. Rev. Lett.* **122**, 023601 (2019).
- [78] V. Dwivedi and V. Chua, Of bulk and boundaries: Generalized transfer matrices for tight-binding models, *Phys. Rev. B* **93**, 134304 (2016).
- [79] S. Sachdev, Quantum phase transitions, *Phys. World* **12**, 33 (1999).
- [80] S. Chen, L. Wang, Y. Hao, and Y. Wang, Intrinsic relation between ground-state fidelity and the characterization of a quantum phase transition, *Phys. Rev. A* **77**, 032111 (2008).
- [81] D. Rossini and E. Vicari, Ground-state fidelity at first-order quantum transitions, *Phys. Rev. E* **98**, 062137 (2018).